

Dual quantum cascade laser trace gas instrument with astigmatic Herriott cell at high pass number

J. Barry McManus,* Mark S. Zahniser, and David D. Nelson

Aerodyne Research, Inc., 45 Manning Road, Billerica, Massachusetts 01821-3976, USA

*Corresponding author: mcmanus@aerodyne.com

Received 4 August 2010; accepted 13 September 2010;
posted 5 November 2010 (Doc. ID 132887); published 20 December 2010

We have developed and demonstrated a high-sensitivity trace gas instrument employing two mid-infrared quantum cascade lasers and an astigmatic Herriott sample cell with up to a 240 m path length. Several aspects of astigmatic Herriott cell optics have been addressed to enable operation at a high pass number (up to 554), including aberrations and pattern selection to minimize interference fringes. The new instrument design, based on the 200 m cell, can measure various atmospheric trace gases, depending on the installed lasers, with multiple trace gases measured simultaneously. Demonstrated concentration noise levels (1 s average) are 40 parts per trillion [(ppt) 10^{-12}] for formaldehyde, 10 ppt for carbonyl sulfide, 110 ppt for hydrogen peroxide (H_2O_2), and 180 ppt for nitrous acid (HONO). High-precision measurements of nitrous oxide and methane have been recorded at the same time as high-sensitivity measurements of HONO and H_2O_2 . © 2010 Optical Society of America

OCIS codes: 080.2740, 120.6200, 140.4780, 300.1030, 300.6340, 300.6360.

1. Introduction

The problems presented by atmospheric trace gas measurements present continuing challenges for laser spectroscopic instrumentation. Atmospheric trace gas measurement problems cover a range of requirements in terms of sensitivity, precision, speed, and specificity. Atmospheric chemistry research presents requirements for very high performance instrumentation, with evolving questions and challenges as the science develops. There is a trend toward resolving questions involving chemicals at very low mixing ratios [of the order of 10^{-12} mole trace gas/mole air, i.e., parts per trillion (ppt) levels] and toward precision measurements at high speed.

The combination of mid-infrared (mid-IR) laser spectroscopy with long path absorption is a technique that can yield high sensitivity and precise trace gas measurements [1–29]. Working in the mid-IR spectral region has the advantage of fundamental transitions with the strongest absorptions. The invention of quantum cascade lasers (QCLs) [30–35]

has been pivotal in the recent development of high-precision mid-IR spectroscopic instrumentation for atmospheric trace gas measurements [4–29]. Instruments based on QCLs have been deployed in field settings to help answer questions posed in atmospheric chemistry research. There has been great progress in moving from cryogenically cooled QCLs [4,5] and detectors to thermoelectrically (TE) cooled QCLs and, more recently, with fully cryogen free systems employing TE-cooled detectors [6–19]. Further improvement in performance has been achieved with the advent of continuous wave (CW) QCLs [20–22,31,32,35]. Multipass cells are used to increase the optical path length through a sample of gas and thereby increase the measurement sensitivity. The absorption line depth is the primary signal in the measurement, and increasing the path length to increase the line depth thus improves the signal-to-noise ratio (SNR), up to some limit (often of the order of 10% absorption depth). For some measurement problems, where the gas concentration is low or the line strength is weak, a multipass cell is essential for achieving the required detection limits.

Aerodyne Research, Inc. has recently developed a new dual-QCL trace gas instrument, which has

0003-6935/11/040A74-12\$15.00/0
© 2011 Optical Society of America

shown significant improvements in sensitivity and precision, in order to continue to contribute to the needs of atmospheric research. The instrument has a multipass cell with 200 m or greater path length and an overall length of ~60 cm. The instrument size is the same as an earlier dual-laser spectrometer with a 76 m path length cell. The 200 m cell design is enabled by several technological developments. The availability of high reflectivity mid-IR mirror coatings (>99.8%) (e.g., LohnStar Optics, Inc.) makes a cell with >400 passes useful. The design is also enabled by the availability of CW QCLs, with high enough power to overcome the dark noise limits of TE cooled detectors. The design is also enabled by a detailed understanding of the optics of the astigmatic Herriott cell, which is a topic of discussions to follow.

In this paper, we will describe several challenges to the use of astigmatic Herriott cells at high pass numbers. These challenges include understanding the basic scaling rules for the cell, selection of optimum circulation patterns, and how to compute precise maps of pattern location in the adjustment space of mirror spacing and twist. We present initial results on the accumulation of aberrations in the cell. We also describe how patterns are selected to reduce the effects of interference fringes. We present the completed design for the cell and the dual-laser instrument and trace gas measurement results.

2. Astigmatic Cell Design Considerations

In this section, we describe some of the design choices for a high pass number astigmatic Herriott cell. The first consideration is the size of the mirrors needed for a given pass number, which is determined by a combination of geometric scaling rules and diffraction. A simple treatment indicates that aberration and diffraction effects should be comparable in determining spot sizes for cells with ~400 to 500 passes. Finally, we address the selection of circulation patterns that are expected to have less problematic interference fringes.

We briefly review how astigmatic Herriott cells work before describing the challenges of pushing to higher pass numbers. The spherical-mirror Herriott cell is a multipass cell configuration that provides easy availability of relatively high pass numbers (~20–100) [36,37]. The beam circulates with a fixed angular advance per pass, producing a circular or elliptical spot pattern on the mirrors. The pass number in the Herriott cell is changed by changing the mirror spacing. The astigmatic Herriott cell uses mirrors that have two different radii of curvature (e.g., a toric surface). The astigmatic Herriott cell produces a spot pattern that is essentially a Lissajous pattern, which appears as a dense set of spots on the cell mirrors with a square- (or diamond-) shaped boundary. The possibility of an astigmatic Herriott cell was mentioned earlier [37], but the design became much more practical with the introduction of the mirror twist for adjustment [38,39]. A combination of the mirror twist and spacing allows access to a wide range of

circulation patterns. Another variation on the astigmatic Herriott cell is to push the astigmatism to the extreme case of cylindrical mirrors [40–42]. Cylindrical mirror cells are described by the same mathematics, and they have the same adjustment method as lower-astigmatism cells [39]. The lower production cost of cylindrical mirrors compared to toroids may be offset by a greater difficulty of alignment.

The simplest description of an astigmatic cell applies when the mirror axes both are aligned on the X and Y axes (i.e., without twist). In that case, the trajectory of a narrow beam of light through the cell, as indicated by the beam spot locations on the mirrors, is sinusoidal in X and Y . The coordinates of the n th spot are given by

$$X_n = A_x \sin(n\theta_x), \quad Y_n = A_y \sin(n\theta_y), \quad (1)$$

where $\theta_x = \cos^{-1}(1 - D/R_x)$, $\theta_y = \cos^{-1}(1 - D/R_y)$, the mirror spacing is D , and the radii of curvature are R_x and R_y . In a typical implementation, an astigmatic Herriott cell is made with a central hole in one mirror, allowing light to be injected and to escape after a prescribed number of passes. When the mirror spacing and radii are arranged so that the beam returns to the starting point and exits after N passes, then

$$\theta_x = \pi N/M_x, \quad \theta_y = \pi N/M_y, \quad (2)$$

for integers, M_x and M_y . Each closed beam circulation pattern can be identified with this set of three integers, $\{N, M_x, M_y\}$. In this simple case, N must be even and there are no factors common to the set, other than 2. When we allow the twist of the mirror axes about the central axis, the circulation advance angles (θ_x, θ_y) are modified, which allows one to adjust the cell for a wide variety of circulation patterns [38,39]. The astigmatic cell can produce an almost bewildering set of patterns, without obvious order. However, a “map” of patterns as a function of spacing and twist reveals a beautiful order and a useful guide to alignment.

A. Pattern and Spot Scaling

A primary concern in designing a higher pass number cell is the scaling of the pattern and the mode size. The most basic scaling rules for the maximum number of passes is determined by the beam circulation pattern, which must fit between the mirror outer radius and the mirror hole radius (except for the input/output beams). This description uses ray optics in the paraxial approximation. The geometry of the spot pattern on the mirror is shown in Fig. 1. The circulation pattern is represented only by the outermost and innermost spots. The size of the circulation pattern is set by the initial aiming onto the back mirror. The radius of the innermost beam spots depends on the particular pattern, and it scales with the pattern size. The finite size of the outer and inner beam spots requires that the pattern outer radius is smaller

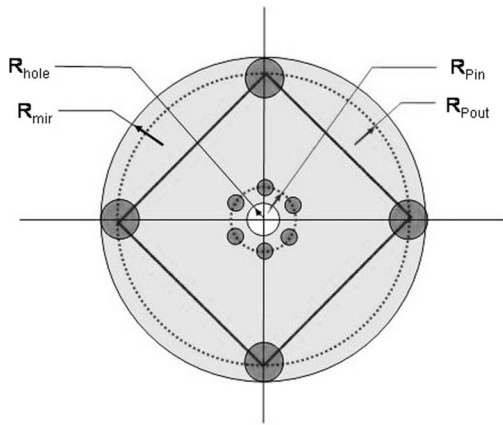


Fig. 1. Geometry of the cell mirror, with pattern boundaries indicated in a dotted circle. The circulation pattern is represented only by the outermost spots (large dots) and innermost spots (small dots). The input/output beam spots at the center of the mirror are not shown.

than the mirror radius, $R_{\text{pout}} < R_{\text{mir}}$, and the pattern inner radius is larger than the hole radius, $R_{\text{pin}} > R_{\text{hole}}$. For a set of patterns with a given pass number, there is a maximum spacing of the inner spots around the coupling hole:

$$R_{\text{pin}} = R_{\text{pout}}\pi/\sqrt{N_p}, \quad (3)$$

where N_p is the number of passes. Alternately, for the number of passes for optimal patterns:

$$N_p = (R_{\text{pout}}\pi/R_{\text{pin}})^2. \quad (4)$$

The clearances and mirror size needed for high performance multipass cells are increased by beam diffraction, which limits the minimum beam size. The effects of diffraction have been examined by calculating the propagation of Gaussian beams (of the lowest order) in the cell, using standard ABC formalism. For simplicity during design considerations, the mirror twist is ignored [42]. Gaussian beam propagation is examined with the cell “matched” or “mismatched.” In the matched case, the beam waist is in the center of the cell and the beam radius increases by a factor of $\sim\sqrt{2}$ at the mirrors (with nearly confocal mirror spacing). In the matched case, the beam spots are nearly the same size and the mirror size is modestly larger than the minimum defined by the pattern geometry. The mismatched case allows the initial beam waist to be smaller and away from the cell center, which leads to variable spot sizes.

We have made a set of comparisons of different matching conditions on the spillover of beams near the coupling hole to check the conditions for the smallest mirrors. We have found that with a modest degree of mismatch, the spot sizes around the coupling hole can be smaller than in the matched-beam case, while the growth of the outer edges of the beam does not force the pattern to be too squeezed at the mirror edge. A smaller mirror set potentially could be

used with some degree of mismatch. However, the question of matching and beam profiles appears again when we discuss aberrations and interference fringes.

B. Astigmatic Cell Aberrations

We have previously presented a detailed description of paraxial propagation in astigmatic cells [39], but with finite off-axis aim-in angle and finite beam size, nonparaxial aberration effects cause deviations from paraxial behavior. The pattern may not close at the predicted conditions, and the output beam may have a larger than expected size. While a detailed examination of aberrations in astigmatic cells is beyond the scope of this paper, we describe some preliminary results based on comparing paraxial matrix propagation and exact geometric calculations of propagation at finite angles. Aberrations are a noticeable effect in simulated high pass number astigmatic cells. An example calculation is shown in Fig. 2. With mirror radii 675.9 and 740 mm, pattern {446, 178, 170} is predicted by paraxial calculations to appear at the mirror separation (D) 467.354 and twist (τ) 13.86°. According to exact calculations, with a finite aim-in angle (0.031, 0.031 radians in x and y), giving a pattern radius of 22 mm (fitting on a 25 mm radius mirror), the pattern best converges at $D = 467.407$, $\tau = 13.869$. Thus the exact mirror spacing differs from the paraxial calculation by 0.05 mm. With a point source at the front mirror and a Gaussian-profile spot at the back mirror (radius 2 mm), the output spot radius (standard deviation) is 0.37 mm. A plot of the first spot and last spot is shown below [Fig. 2(a)]. When the input is a ring of 2 mm radius, the output is a distorted ring, with standard deviation of 0.25 mm [Fig. 2(b)].

In simulations of numerous patterns and mirror radii, we are developing a clearer picture of the aberration effects in the astigmatic Herriott cell, but a full exposition of results will be presented in a later publication. Results to date indicate the aberrations accumulate linearly with the number of passes and depend only weakly upon the patterns and mirror spacing in relation to the radii of curvature. The distortions of the output spot increase as the square of the beam spread angle, which means that the least

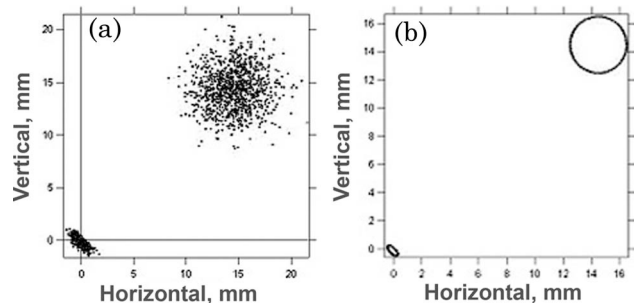


Fig. 2. Computed spot distortion due to aberration in the cell. The input spot at the back of the cell is shown at the upper right in both panels, and the spot that returns to the origin is at the lower left.

spreading angle input beam should be used. For the cases studied to date, the aberrations for 400 to 500 pass cells will produce excess beam sizes that are on the same order of size as the diffraction limit.

C. Interference Fringes

A concern for high pass number multipass cells is the possibility of scattered light generating interference fringes, which limit the SNR improvement provided by the long path. There is often a trade-off between minimizing the cell volume and minimizing the interference fringes. Minimizing the cell volume is important to reduce the overall instrument size and to reduce the amount of time and energy needed to exchange gas. As many multipass cells are operated at reduced pressure (to reduce pressure broadening), reducing the volume reduces the size of the pump, which can be a large part of the system power requirement. Scattering of light on the mirror surfaces can cause some light to exit the cell early or late and interfere with light following the main path. Interference fringes can be reduced by making the mirrors larger to more widely separate beam spots, thereby increasing the cell volume. Various other methods can be used to reduce interference fringes, such as vibrating the mirrors to average fringes, keeping the mirrors clean to minimize scatter, and placing a baffle in the coupling hole to reduce input/output scatter.

Another possible method of reducing problematic interference fringes in an astigmatic Herriott cell is to select the circulation pattern to minimize overlap of the beam spots with small pass number differences. In absorption measurements, the most problematic fringes are those with a free spectral range comparable to or somewhat greater than the width of the absorption line. The degree of interference by a fringe in the measurement of a low pressure absorption line can be estimated from the overlap integral (I) of a Gaussian profile (centered at frequency ν_o , with unit depth and frequency width ω) and a sinusoid (amplitude, $e A$, and free spectral range F_s):

$$I = \int_{-\infty}^{\infty} \exp(-[(\nu - \nu_o)/\omega]^2) A \sin(2\pi\nu/F_s + \varphi) d\nu \\ = A 2^{1/2} \sin(\varphi) \exp(-(\pi\omega/F_s)^2). \quad (5)$$

The fringe effect is strongly suppressed for $F_s \ll \pi\omega$. When measuring at a pressure of $\sim 1/25$ atmosphere, a typical small-molecule absorption width is $\sim 0.005 \text{ cm}^{-1}$ (HWe⁻¹).

Thus, we want $F_s \ll 0.016 \text{ cm}^{-1}$ or a generating length of $L = 1/F_s \gg 600 \text{ cm}$. The lowest frequency fringes, corresponding to small pass number differences in the cell, are the ones to minimize first. We have used this consideration in selection of circulation patterns for the 200 m cell, and we show results later in this paper.

Because we lack a fundamental prescription for the selection of preferred patterns, we have surveyed the properties of all possible patterns (up to a maximum pass number of 500). Each pattern is specified by a unique set of three numbers $\{N, M_x, M_y\}$, where N is the pass number, and M_x and M_y are winding numbers, both less than N . Up to $\sim 10^8$ possible patterns might be considered with $N < 500$. Several fundamental selections can be applied immediately to reduce the number of possibilities. Because the same hole is used for entrance and exit, N is even. We employ "complete patterns" for better filling and higher symmetry, so M_x and M_y are even [38,39]. The set of pattern numbers can have no common factors for the set, other than 2. Patterns with x and y exchanged are fundamentally the same, so we can restrict the survey to $M_y < M_x$. Patterns with $M'_x = N - M_x$ are the same as those with M_x , and patterns with $M'_y = N - M_y$ are the same as those with M_y , so we can further restrict the survey to $0 < M_x < N/2$. The list of patterns to examine finally is reduced to 587,330. We collected statistics for all of these remaining patterns by calculating the set of beam center coordinates according to Eqs. (1) and (2), which correspond to idealized cells without twist.

Patterns were selected for further examination if the distance of the inner spots from the coupling hole was more than 85% of the maximum possible spacing at that pass number. This left 101,331 patterns to examine in more detail. The reduced set of 101,331 patterns occupies 1/8 of the full solution space. A plot with the location of all 810,648 patterns with wide hole spacing is shown in Fig. 3. The positions are plotted in terms of the fractions $M_x/N, M_y/N$, which correspond to the advance angles (θ_x, θ_y) divided by π . For a spherical mirror resonator, different mirror separations correspond to different points on the main diagonal of the plot. Confocal separation corresponds to the center of the plot, at the point (1/2, 1/2). The resonator mirrors would be at zero separation at the (0, 0) corner, and at twice confocal at (1, 1). The resonator is unstable beyond (1, 1). Astigmatic mirrors make available a set of patterns in a wedge-shaped zone around the main diagonal. The available patterns for a mirror set with 9% difference in radii, such as we use in our final cell design, are in the region between the two gray curves in Fig. 3.

To identify patterns with the potential for good low-frequency fringe performance, during the pattern survey we computed the minimum spacing between spots for a set of low pass number differences. Specifically, for each pattern $\{N, M_x, M_y\}$, on a $+/-1$ square, we calculated the minimum spacing between all beam spots i and j , where $|i - j| = \Delta$, giving the sets $R_{\min}(\Delta : N, M_x, M_y)$. The relevant spots are on the same mirror, so Δ is even. The front and back mirror patterns are very similar, so the spacings for just one mirror are calculated. The values for $R_{\min}(\Delta : N, M_x, M_y)$ for $\sim 10^5$ patterns are plotted in Figs. 4 and 5, with pattern locations plotted as

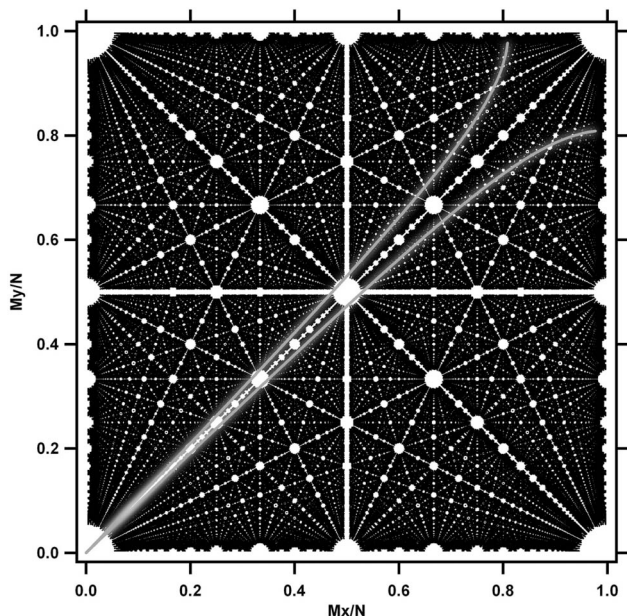


Fig. 3. Patterns with good hole spacing throughout the available solution space are plotted as black points. The solution space is represented with the range from 0 to 1 in two dimensions. The patterns available with mirrors with 9% astigmatism are between the two gray diagonal curves.

$(M_x/N, M_y/N)$, and the color indicates the minimum spot separation at a given Δ .

The maps of $R_{\min}(\Delta : N, M_x, M_y)$ show striking regularities, with bands in x and y with near zero separations and zones between the bands where there are patterns with good separation. The zero-separation bands are at x or $y = 2K/\Delta$, where K is an integer.

That regularity is consistent with Eqs. (1) and (2), given that the advance angles for return to a given mirror are $2n\theta_{x,y} = 4\pi nK/\Delta$. Then we have, for example, with the x coordinate:

$$R_{\min}(\Delta : N, M_x, M_y) = \text{Min}\{(X_{n+\Delta} - X_n)\} \\ \times \text{Min}\{\sin((n + \Delta)4\pi K/\Delta) - \sin(n4\pi K/\Delta)\}, \quad (6)$$

$$\sin((n + \Delta)4\pi K/\Delta) - \sin(n4\pi K/\Delta) = 2 \cos[(2n + \Delta) \\ \times 2\pi K/\Delta] \sin(2\pi K) = 0. \quad (7)$$

The Δ difference spot separations at these fractional coordinates (in one dimension) are all zero. On a line where $2n\theta_x = 4\pi nK/\Delta$, the x values for the spots fall on only a few $(\Delta/2)$ values, so there is a high likelihood of spots that are also closely spaced in y . In contrast, regions in the adjustment space for the cell where we can expect to find patterns with wide spacing between spots at low pass numbers are zones centered at

$$x = (2J + 1)/\Delta, \\ y = (2K + 1)/\Delta, \quad (8)$$

for integers J and K . In order to find patterns with widely separated spots at several low pass number

differences, we need to find regions where Eq. (7) can be satisfied for multiple Δ s. As the number of Δ s increases, we see a shrinking region of adjustment space where such multiple constraints can be satisfied. Nevertheless, there are regions where wide separation for $\Delta = 2$ to 8 can be achieved, to produce cells with low fringe amplitudes for path length differences up to 8. When we simultaneously consider multiple low-order fringes, the zones where both x and y fractions are close to odd multiples of $1/\Delta$ are near the corners of the solution space.

After the survey of patterns, several more steps are needed for final selection of the cell setup conditions. For the present design project, we have limited ourselves to patterns available with the radii of curvature of the mirrors we presently use in AMAC-100 and AMAC-200 cells (675.9 and 740 mm), with a mirror spacing range of 40 to 50 cm. This places us in the region of solution space where $\theta_x \approx 1.26$, $\theta_y \approx 1.2$, or in terms of the fraction coordinates used above, $F_x \approx 0.40$, $F_y \approx 0.383$. Thus, from the arguments presented above, we expect the first strong cell fringes to be at a 10 pass difference. An additional choice is that the mirror twist should be $\sim 5^\circ$ – 20° , because with too much twist the pattern becomes diamond shaped and does not fill the mirror well, and with too little twist there is little latitude for adjustment. It is advantageous to have good patterns with various lengths close together in adjustment space, to allow flexibility in path length. Also, it should be relatively easy to “navigate” through the adjustment space to find the high pass pattern.

We have reevaluated the potential for fringe generation for selected candidate patterns by using the Gaussian beam propagation simulations described above. We calculate the total overlap strength at specified pass number differences from computed field distributions with specified matching conditions. Generally we see that the lowest fringe overlap strengths are achieved when we used “matched” beams in the cell. The use of mismatched beams to more tightly squeeze spots on the mirror does not seem to be an advantage in light of the worsened fringe performance. The general characteristics of some of the patterns are listed in Table 1. Gaussian beam overlap strengths for these patterns are given in Table 2, where the strengths are calculated with a matched beam at $6\mu\text{m}$, mirror separation of 47 cm, and mirror radius of 3.8 cm. The calculated overlap strengths shown in Table 2 represent a general guide to which fringe lengths are expected to be stronger. Changing the matching conditions or alignment into the cell changes the values of the overlap strengths, but the ranking of strengths is fairly robust. For all of these patterns, the strongest spot overlaps are at a 10 pass separation, indicating the strongest fringes will be at a 10 pass difference (~ 470 cm generating length, free spectral range $\sim 0.0021\text{ cm}^{-1}$).

Exact (geometric) propagation expressions are used to calculate a map of pass number versus mirror separation and twist, for selected regions (in D and τ)

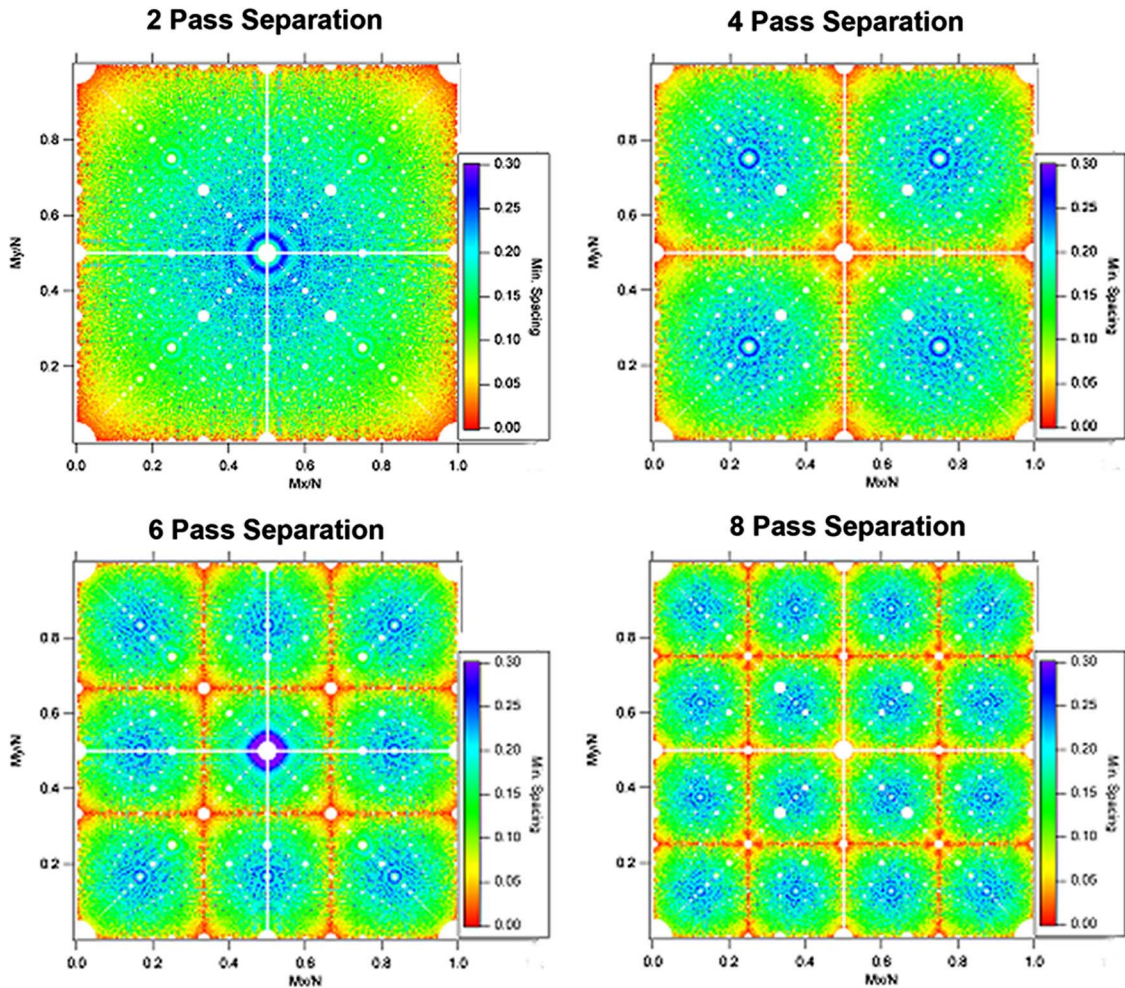


Fig. 4. (Color online) The same patterns as in Fig. 3 are plotted with color according to the closest spot separation at a given pass number difference.

with favorable patterns, as shown in Fig. 5. Predicted mirror spot patterns also can be calculated to use as an aid to pattern identification as we move through the adjustment space. An example of calculated mirror spots for pattern [434, 174, 166] is shown in Fig. 6(a). The calculated spot radii decrease with pass number to simulate dimming, but we have not attempted to portray the asymmetrical focusing of the spots. An observed pattern on the input cell mirror is shown on the right-hand side of Fig. 7, with a good match to the calculation.

3. Final Cell and Instrument Design

The optomechanical design of the 200 m cell is a departure from earlier astigmatic Herriott cell designs at Aerodyne Research, Inc., because this cell

is based on a solid aluminum tube rather than a glass tube. This design is expected to be more rigid, with reduced thermal gradients. This design also has both mirrors on kinematic mounts, allowing easier removal or replacement. The back mirror assembly is built as a large cylindrical plug that can be adjusted in spacing and angle, then locked into the tube bore. The cell has 7.8 cm diameter toroidal-surface mirrors at a separation of ~ 47 cm, giving an active volume of 2.1 liters. Path lengths of up to 240 m (with 554 passes) have been demonstrated.

The internal alignment of this cell presents some difficulties, due to the aluminum tube and the high pass numbers. In prior designs with glass tubes, one can see the pattern on the mirrors with a visible trace

Table 1. Identification of Several Candidate High Pass Number Patterns

Pattern [N, M_x, M_y]	Mirror Separation (cm)	Mirror Twist ($^\circ$)	Path Meters
[422, 170, 162]	47.42	11.13	200.1
[434, 174, 166]	47.07	12.59	204.3
[554, 222, 212]	47.06	13.8	260.7

Table 2. Overlap Strengths Versus Pass Number Difference^a

Pattern	2	4	6	8	10
[422, 170, 162]	0	0	0.029	0	9.2
[434, 174, 166]	0	0	0.02	0	20.2
[554, 222, 212]	0	0.1	0.37	0	34.5

^aCalculated for matched (center focus) Gaussian beams, wavelength $6\ \mu\text{m}$, mirror radius 38 mm.

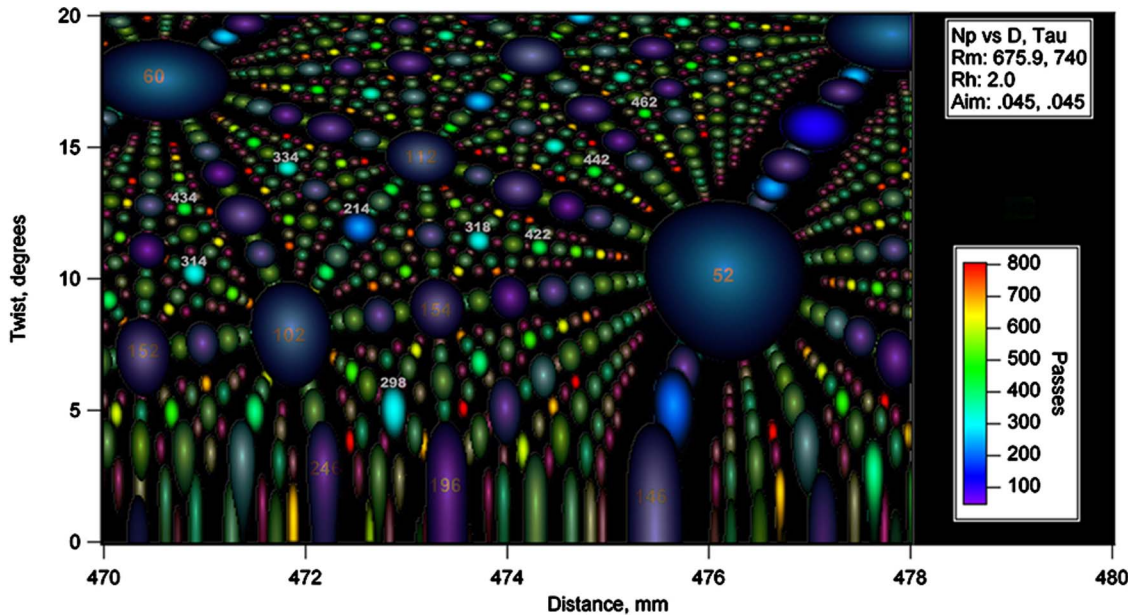


Fig. 5. (Color online) Map of pattern locations as a function of mirror spacing and twist for a range of setup conditions close to several candidate patterns. The map is calculated using nonparaxial ray tracing with a single ray at a finite angle. The map shows nearly circular zones, each representing the location of a different pattern. The pass number is indicated by color. The error in the return location of the final ray is indicated by the darkened tone at the edge of each zone. The patterns with the beam exiting in the wrong direction (incomplete patterns) are indicated with a gray color.

laser. Here we observe the pattern on the mirrors with a borescopelike viewer inserted into the gas in/out ports. The high pass number results in a smaller zone of spacing and twist, over which the pattern is found. A precision translation and rotation jig is attached to the rear mirror assembly to facilitate precision alignment. The jig is removed once the rear mirror assembly is locked in place. In practice, we align the cell by stepping from lower to higher number patterns, using the map (e.g., Fig. 5) as a guide. The spacing and twist differences between patterns may be more easily verified than the absolute spacing and twist. The final path length has been verified using optical propagation delay with modulated lasers.

The optical design of the new dual instrument is based on our previous dual instrument with a 76 m cell, with several innovations that allow placement of a new 200 m cell on the 43 cm \times 64 cm table. A diagram of the optical table is shown in Fig. 7. The

optical design of the spectrometer has been described in some detail in a recent publication [43], so we present here only a brief description.

The optical train begins with the two QCLs mounted on Peltier coolers in sealed housings. Laser light is collected by a pair of 15 \times Schwarzschild objectives and then combined with a dichroic beam splitter and focused through a pinhole. The segment of the optical train before the pinhole has several alignment aids built in. A visible trace laser that is coaligned with one of the IR laser beams allows visualizing the optical path all the way to the detector. Both IR beams reflect from visible-IR dichroics, which allows us to have viewing points for both lasers. A drop-in eyepiece placed behind the dichroics,

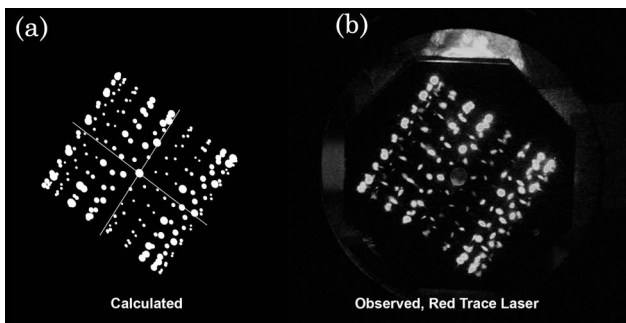


Fig. 6. (a) Calculated and (b) observed mirror spots for the pattern {434, 174, 166}.

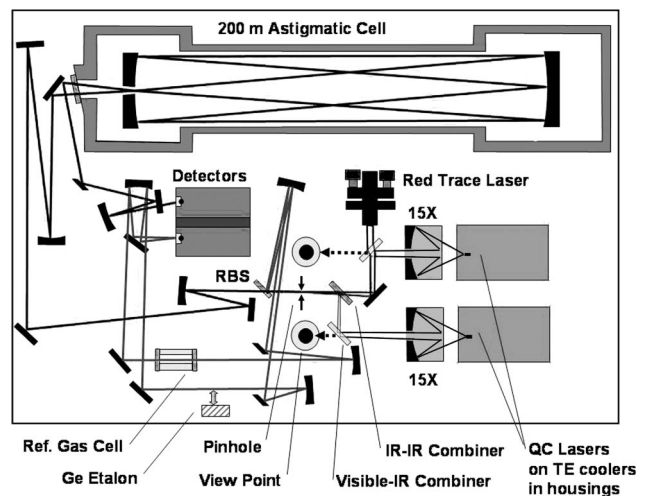


Fig. 7. Diagram of the optical module for our new instrument.

combined with the 15× objectives, gives 15× views of the laser faces. Past the pinhole, the combined beam is reimaged into the multipass cell in two steps, which increases the magnification and thus reduces the beam angle.

The dual-laser instrument has two reference paths, derived from reflection from the two faces of a wedged beam splitter. There is a “reference locking” path that contains one or two short gas cells with high concentrations of the gases of interest. Fitting to absorption lines produced by the gas cell allows us to lock the laser frequencies to specific absorption lines. The other reference path may be used for power normalization, or a Ge etalon may be flipped into the path in order to measure the laser tuning rate. An electromagnetically actuated flag may be flipped to allow either reference beam to reach the single reference detector.

4. Measurement Results

Some of our best instrument performances to date have been demonstrated with the new dual-laser design. We have tested the instrument design with both TE-cooled and LN₂-cooled detectors and two different pairs of CW QCLs. The performance data presented below are actually from two different versions of the same design. The first instrument has lasers at 1765 cm⁻¹ (5.66 μm) and 2052 cm⁻¹ (4.87 μm) for measuring HCHO and OCS, respectively. That instrument has already been deployed in a field measurement campaign, CALNEX, during May–June 2010 [44]. The second instrument is configured for measuring HONO and H₂O₂ with lasers operating at 1275 and 1286 cm⁻¹, respectively.

Our general data analysis method is direct absorption with sweep integration and fitting to model absorption profiles. The laser is repeatedly swept at high frequency (~1–5 kHz) across a narrow spectral range (~0.5 cm⁻¹), with a shutoff period (to measure laser power) at the end of each sweep. The data analysis program TDLWintel [10] controls laser sweep, data acquisition, and analysis. Detected signals are synchronously averaged and then fit, using HITRAN [45] parameters with measured pressure and temperature to determine mixing ratios. The same control and analysis program can be used for either pulsed or CW lasers.

A. Cell Fringe Spectra

We have examined the spectra recorded from the instrument with the cell set to different patterns to determine interference fringe strengths and frequencies and to compare to expectations from the pattern selection process. In order to determine the fringe content of the spectra, we first preprocess the spectra by a double normalization, dividing each spectrum by its average, and then dividing by the average normalized spectrum for the whole set. This preprocessing removes the stationary baseline structure and highlights changes in the normalized spectra. The frequency content is analyzed using

the nonuniform laser frequency scale, in a Lomb power spectrum algorithm. Cell fringes appear as peaks in the spectral power at even multiples of the cell base length. Fringes generated elsewhere in the optical train generally will not be at multiples of the base length. Recorded spectra also generally contain some amount of narrowband electronic pick-up, which will contribute broad features to the Lomb power spectra. Conversely, a fast Fourier transform (FFT)-based analysis with uniform frequency spacing shows narrowband electronic noise as sharp features and cell fringes as broad features. The extent to which the Lomb and FFT analyses are distinct depends on the degree of nonlinearity in the laser tuning.

Interference fringe power spectra are shown in Figs. 8–10 for the cell set to 422, 434, and 554 passes, respectively. We have done the fringe analysis under a variety of conditions, and we have observed that the cell fringe levels depend on cell aim-in and other alignments in the system. The examples shown in Figs. 8–10 are rather typical of spectra observed during actual measurements. In all cases, the 10 pass fringe is the strongest cell fringe, as predicted by the overlap calculations. The overlap calculations also reproduce the observed ordering of strengths. The actual observed ratios of fringe strengths are not well predicted by the overlap strengths. We also observed strong low-frequency fringes originating from the optical train outside the cell. Those were usually the most problematic for instrument stability.

B. Formaldehyde and Carbonyl Sulfide Measurements

The first concentration measurement performance results are presented for the instrument configured with two TE-cooled CW DFB-QCLs at ~1765 cm⁻¹ (5.66 μm) and ~2052 cm⁻¹ (4.87 μm) for measuring HCHO (1764.902 cm⁻¹) and OCS (2052.256 cm⁻¹), respectively. There is an extensive literature on the use of tunable mid-IR lasers to measure HCHO [5,14,23–25] and OCS [27–29]. Our instrument also measures formic acid (HCOOH, 1765.01 cm⁻¹) and carbon dioxide (CO₂, 2052.096 cm⁻¹) at the same

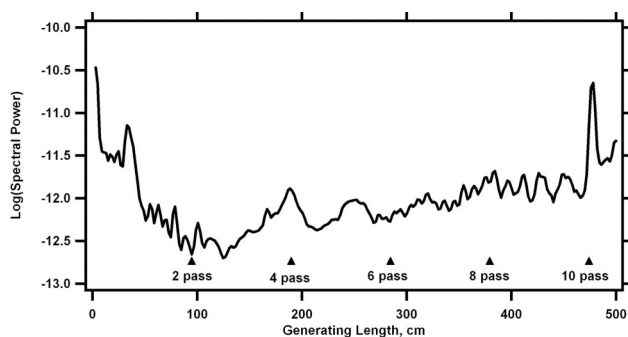


Fig. 8. Average power spectrum derived from spectra recorded with the dual-laser instrument where the cell was set to 422 passes. Generating lengths corresponding to even multiples of the cell base length are indicated by triangles. Here, the only clear cell fringe is at 10 passes.

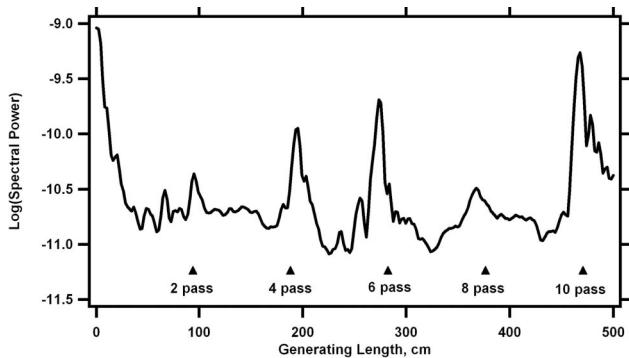


Fig. 9. Average power spectrum derived from spectra recorded with the dual-laser instrument where the cell was set to 434 passes. Generating lengths corresponding to even multiples of the cell base length are indicated by triangles. Here, there are clear cell fringes at 2, 4, 6, and 10 passes. This may be a case where the alignment into the cell is poor.

time as HCHO and OCS. For the data presented below, we used the LN₂ detector. The short-term noise with the TE-cooled detectors was similar to that achieved with the LN₂ detector, but the LN₂ detector had better stability and less saturation, which gave better results in terms of absolute concentrations.

This instrument was used to measure HCHO and OCS in marine environments during the CALNEX [44] campaign in May and June of 2010. In Fig. 11, we show an Allan variance plot [46] for a measurement of formaldehyde onboard the research ship Atlantis. Background spectra were collected every 10 min for subtraction from subsequent measured spectra. The 1 s HCHO concentration noise was 44 ppt. At the Allan variance minimum, with 100 s averaging, the HCHO concentration noise was 10 ppt. For the simultaneous formic acid (HCOOH) measurement, the 1 s noise was 41 ppt and the Allan variance minimum noise at 15 s was 15 ppt. For the simultaneous OCS measurement, the 1 s noise was 8 ppt and the Allan variance minimum at 50 s was 2 ppt. These results are summarized in Table 3. While the concentration noise for OCS was better than for HCHO, OCS is a much stronger absorber

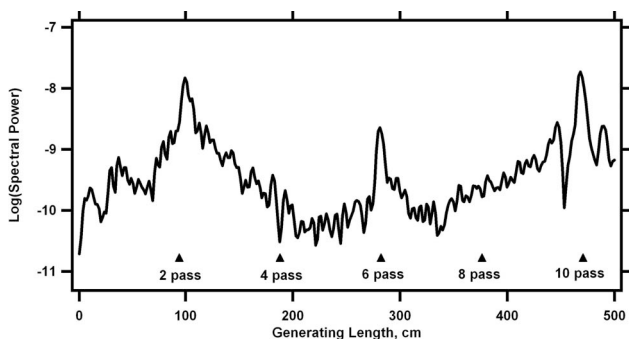


Fig. 10. Average power spectrum derived from spectra recorded with the dual-laser instrument where the cell was set to 554 passes. Generating lengths corresponding to even multiples of the cell base length are indicated by triangles. Here, there are clear cell fringes at 6 and 10 passes. The peak close to 2 passes is at 100 cm and involves the optical train outside the cell.

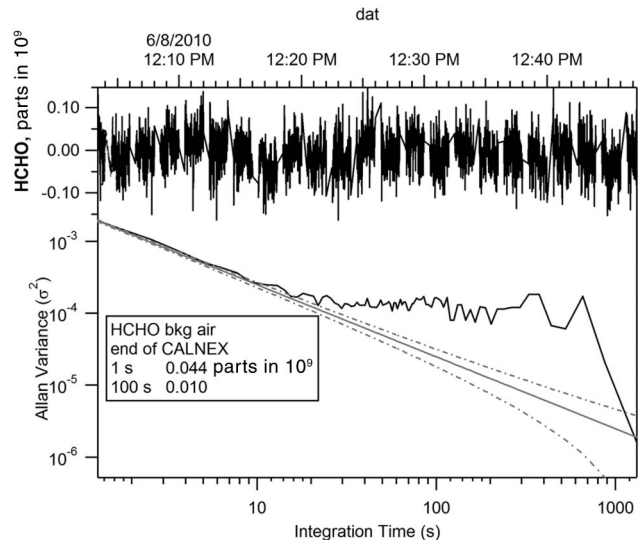


Fig. 11. Allan variance plot for HCHO measured with the dual-laser instrument aboard the research ship Atlantis during the CALNEX experiment.

(~11×) than HCHO. The absorption noise, therefore, was lower for the HCHO measurement ($\sim 4.5 \times 10^{-6}$), compared to the OCS measurement (1.5×10^{-5}).

C. Hydrogen Peroxide, Nitrous Acid, Nitrous Oxide, and Methane

The second set of concentration measurement performance results is presented for the instrument configured with two TE-cooled CW DFB-QCLs, at $\sim 1277 \text{ cm}^{-1}$ ($7.83 \mu\text{m}$) and $\sim 1283 \text{ cm}^{-1}$ ($7.79 \mu\text{m}$) for measuring nitrous acid (HONO, 1277.113 cm^{-1}) and hydrogen peroxide (H_2O_2 , 1283.326 cm^{-1}), respectively. These gases are difficult to measure because they are weak absorbers and their atmospheric concentrations are low. At the same time, the instrument measures nitrous oxide (N_2O , 1277.235 and 1283.374 cm^{-1}) and methane (CH_4 , 1283.381 cm^{-1}). For most of the data collected with this instrument, the absorption cell is set to a pattern with 554 passes, giving a total absorption path length of 260 m. For the data presented below, we used a TE-cooled

Table 3. Summary of Noise Results for the Dual Laser Instrument with 200 m Cell^a

Measured Gas	1 s Noise ppt	Allan Variance Minimum	
		Average Time (s)	Noise, Standard Deviation, ppt
HCHO	44	100	10
HCOOH	41	15	15
OCS	8	50	2.0
CO ₂	220 (parts in 10 ⁹)	—	—
HONO	160	100	16
H ₂ O ₂	100	100	12
N ₂ O	88	35	33
CH ₄	400	30	190

^aThe first group of results is with lasers at 1765 and 2052 cm^{-1} and with a LN₂ cooled detector. The second set of results is with lasers at 1275 and 1286 cm^{-1} and with a TE-cooled detector.

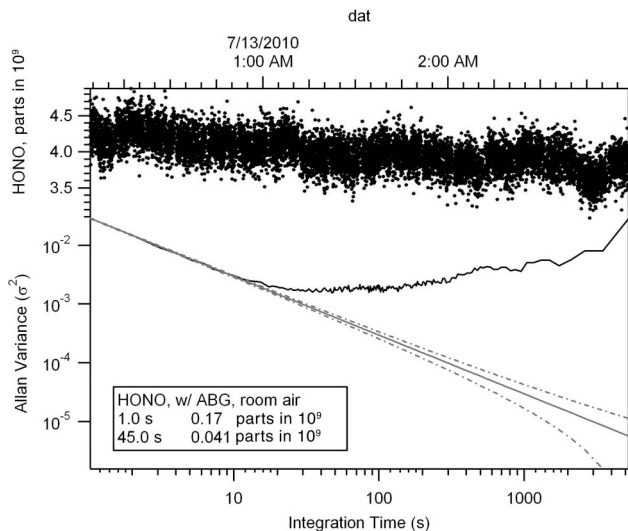


Fig. 12. Allan variance plot for HONO measured in the laboratory, in a sample with a near-zero concentration.

detector. In Fig. 12 we show an Allan variance plot for a measurement of nitrous acid in a sample gas containing a near-zero concentration. Background spectra were collected every 10 min for normalization of subsequent measured spectra. The 1 s HONO concentration noise was 160 ppt. At the Allan variance minimum, with 100 s averaging, the HONO concentration noise was 16 ppt. For the simultaneous hydrogen peroxide measurement, the 1 s noise was 100 ppt and the 100 s noise was 12 ppt. These results are summarized in Table 3.

As part of the process of determining HONO and H_2O_2 concentrations, we fit all the significant lines in the spectra, which, in this case, includes lines from N_2O and CH_4 . The concentration noise results for N_2O and CH_4 were surprisingly good, given that they were not the main focus of this measurement. The 1 s noise for N_2O was 88 ppt, or $\sim 3 \times 10^{-4}$ of ambient concentration [typically 320 parts per billion by volume (ppbv)]. The 1 s noise for CH_4 was 400 ppt, or $\sim 2 \times 10^{-4}$ of ambient concentration (typically 1800 ppbv). Thus, while performing high-sensitivity measurements of HONO and H_2O_2 , we get high-precision measurements of N_2O and CH_4 at no additional cost.

5. Conclusions

An extensive discussion of design considerations for an astigmatic Herriott cell at high pass numbers has been presented. The basic geometric scaling rules set the maximum number of passes for a given mirror and hole radius, assuming no reflection loss. The limits of beam size due to diffraction reduces the available number of passes for a given mirror size. Out of the large number of possible circulation patterns, we can select better ones based on accessibility with a given set of mirrors and clearance of the innermost spots from the coupling hole.

We have presented an additional pattern selection criterion, based on the wide spacing of the beam

spots at low pass number differences, in order to reduce the lowest frequency interference fringes that most influence absorption measurements. A survey of spacing properties in a large number of patterns shows where to find patterns with wide spacing at multiple pass number differences. Given the constraints of using an existing set of mirror radii and a range of spacing, we developed a list of patterns expected to have good fringe properties at pass numbers of 422 to 554. Several of the selected patterns have been utilized in a new absorption cell design. We found general agreement with expectations regarding interference fringes produced by scattering in the cell, in that the first strong fringe was at a 10 pass difference.

The new cell, which employs the selected patterns, has been used to provide 200 to 260 m of absorption path length in a compact design. The cell has been aligned by using a precision adjuster and borescope viewer, plus a map of patterns and calculated mirror spot patterns for comparison. The path length has been confirmed with optical delay measurements and with consistency of the spectroscopic determination of gas concentrations. Aberration effects are noticeable at these high pass numbers, but with narrow beams the effects do not appear to limit performance. High-sensitivity and high-precision trace gas measurements have been demonstrated with the new cell design.

A dual-QCL instrument has been designed to use the new absorption cell. Very high sensitivity has been demonstrated with two different instruments of this same design. One such instrument has already been used in the CALNEX field measurement campaign. Demonstrated 1 s noise levels range from 160 ppt for weak absorbers (e.g., HONO) to 8 ppt for strong absorbers (e.g., OCS). At the same time as high-sensitivity measurements are made of reactive gases, high-precision measurements may be made of the stable gases in the atmosphere.

In our continuing work, we plan to apply the dual-laser instrument design to the measurement of other trace gases, especially where very high sensitivity or precision is required. One area of promising application is in the measurement of the isotopic composition of atmospheric gases (other than CO_2). We also plan to improve the ruggedness and thermal stability of the instrument. We will present a more detailed discussion of the modeling of cell interference fringes and aberrations in future publications.

We thank Scott Herndon for his work with our latest instrument design on the National Oceanic and Atmospheric Administration (NOAA) ship Atlantis. We thank the United States Department of Commerce, NOAA Earth System Research Laboratory, for the opportunity to participate in the CALNEX campaign. We thank Ryan McGovern, Dan Glenn, and Stanley Huang at Aerodyne, who contributed to the electronic and optical engineering and fabrication. We thank Will Lohness of LohnStar Optics, Inc. for providing the high-reflectivity mirror coatings.

Funding for this work has been provided in part under the Small Business Innovation Research (SBIR) program of the United States Department of Energy (DOE) and by the National Oceanic and Atmospheric Administration (NOAA), United States Department of Commerce.

References

1. R. F. Curl, F. Capasso, C. Gmachl, A. A. Kosterev, J. B. McManus, R. Lewicki, M. Pusharsky, G. Wysocki, and F. K. Tittel, "Quantum cascade lasers in chemical physics," *Chem. Phys. Lett.* **487**, 1–18 (2010).
2. F. K. Tittel, Y. Bakhirkin, A. A. Kosterev, and G. Wysocki, "Recent advances in trace gas detection using quantum and interband cascade lasers," *Rev. Laser Eng.* **34**, 275–282 (2006).
3. J. Röpcke, S. Welzel, N. Lang, F. Hempel, L. Gatilova, A. Rousseau, and P. B. Davies, "Diagnostic studies of molecular plasmas using mid-infrared semiconductor lasers," *Appl. Phys. B* **92**, 335–341 (2008).
4. C. R. Webster, G. J. Flesch, D. C. Scott, J. E. Swanson, R. D. May, W. S. Woodward, C. Gmachl, F. Capasso, D. L. Sivco, J. N. Baillargeon, A. L. Hutchinson, and A. Y. Cho, "Quantum-cascade laser measurements of stratospheric methane and nitrous oxide," *Appl. Opt.* **40**, 321–326 (2001).
5. C. L. Schiller, H. Bozem, C. Gurk, U. Parchatka, R. Königstedt, G. W. Harris, J. Lelieveld, and H. Fisher, "Applications of quantum cascade lasers for sensitive trace gas measurements of CO, CH₄, N₂O, and HCHO," *Appl. Phys. B* **92**, 419–430 (2008).
6. A. A. Kosterev, F. K. Tittel, R. Köhler, C. Gmachl, F. Capasso, D. L. Sivco, A. Y. Cho, S. Wehe, and M. G. Allen, "Thermoelectrically cooled quantum-cascade laser-based sensor for the continuous monitoring of ambient atmospheric carbon monoxide," *Appl. Opt.* **41**, 1169–1173 (2002).
7. W. H. Weber, J. T. Remillard, R. E. Chase, J. F. Richert, F. Capasso, C. Gmachl, A. L. Hutchinson, D. L. Sivco, J. N. Baillargeon, and A. Y. Cho, "Using a wavelength-modulated quantum cascade laser to measure NO concentrations in the parts-per-billion range for vehicle emissions certification," *Appl. Spectrosc.* **56**, 706–714 (2002).
8. A. A. Kosterev, R. F. Curl, F. K. Tittel, R. Köhler, C. Gmachl, F. Capasso, D. L. Sivco, and A. Y. Cho, "Transported automated ammonia sensor based on a pulsed thermoelectrically cooled QC-DFB laser," *Appl. Opt.* **41**, 573–578 (2002).
9. A. A. Kosterev, and F. K. Tittel, "Chemical sensors based on quantum cascade lasers," *IEEE J. Quantum Electron.* **38**, 582–591 (2002).
10. D. D. Nelson, J. H. Shorter, J. B. McManus, and M. S. Zahniser, "Sub-part-per-billion detection of nitric oxide in air using a thermoelectrically cooled mid-infrared quantum cascade laser spectrometer," *Appl. Phys. B* **75**, 343–350 (2002).
11. J. B. McManus, D. D. Nelson, J. H. Shorter, and M. S. Zahniser, "Quantum cascade lasers for open- and closed-path measurement of atmospheric trace gases," *Proc. SPIE* **4817**, 22–33 (2002).
12. D. D. Nelson, J. B. McManus, S. Urbanski, S. Herndon, and M. S. Zahniser, "High precision measurements of atmospheric nitrous oxide and methane using thermoelectrically cooled mid-infrared quantum cascade lasers and detectors," *Spectrochim. Acta A* **60**, 3325–3335 (2004).
13. R. Jimenez, S. Herndon, J. H. Shorter, D. D. Nelson, J. B. McManus, and M. S. Zahniser, "Atmospheric trace gas measurements using a dual quantum-cascade laser mid-infrared absorption spectrometer," *Proc. SPIE* **5738**, 318–330 (2005).
14. S. C. Herndon, M. S. Zahniser, D. D. Nelson, J. H. Shorter, J. B. McManus, R. Jiménez, C. Warneke, and J. A. de Gouw, "Airborne measurements of HCHO and HCOOH during the New England Air Quality Study 2004 using a pulsed quantum cascade laser spectrometer," *J. Geophys. Res.* **112**, D10S03 (2007).
15. P. M. Chu, D. D. Nelson, M. S. Zahniser, J. B. McManus, Q. Shi, and J. C. Travis, "Towards realization of reactive gas amount of substance standards through spectroscopic measurements," *IEEE Trans. Instrum. Meas.* **56**, 305–308 (2007).
16. J. B. McManus, J. H. Shorter, D. D. Nelson, M. S. Zahniser, D. E. Glenn, and R. M. McGovern, "Pulsed quantum cascade laser instrument with compact design for rapid, high sensitivity measurements of trace gases in air," *Appl. Phys. B* **92**, 387–392 (2008).
17. D. D. Nelson, J. B. McManus, S. C. Herndon, M. S. Zahniser, B. Tuzson, and L. Emmenegger, "New method for isotopic ratio measurements of atmospheric carbon dioxide using a 4.3 μm pulsed quantum cascade laser," *Appl. Phys. B* **90**, 301–309 (2008).
18. B. Tuzson, J. Mohn, M. J. Zeeman, R. A. Werner, W. Eugster, M. S. Zahniser, D. D. Nelson, J. B. McManus, and L. Emmenegger, "High precision and continuous field measurements of δ¹³C and Δ¹⁸O in carbon dioxide with a cryogen-free QCLAS," *Appl. Phys. B* **90**, 415–458 (2008).
19. J. B. McManus, D. D. Nelson, and M. S. Zahniser, "Long-term continuous sampling of ¹²CO₂, ¹³CO₂ and ¹²C¹⁸O¹⁶O in ambient air with a quantum cascade laser spectrometer," *Isotopes Environ. Health Stud.* **46**, 49–63 (2010).
20. M. S. Zahniser, D. D. Nelson, J. B. McManus, S. Herndon, E. Wood, J. H. Shorter, B. Lee, G. Santoni, R. Jimenez, and B. Daube, "Infrared QC laser applications to field measurements of atmospheric trace gas sources and sinks in environmental research: enhanced capabilities using continuous wave QCLs," *Proc. SPIE* **7222**, 72220H (2009).
21. D. D. Nelson, J. B. McManus, S. C. Herndon, J. H. Shorter, M. S. Zahniser, S. Blaser, L. Hvozدارa, A. Muller, M. Giovannini, and J. Faist, "Characterization of a near-room temperature, continuous-wave quantum cascade laser for long-term, unattended monitoring of nitric oxide in the atmosphere," *Opt. Lett.* **31**, 2012–2014 (2006).
22. J. B. McManus, D. D. Nelson, S. C. Herndon, J. H. Shorter, M. S. Zahniser, S. Blaser, L. Hvozدارa, A. Muller, M. Giovannini, and J. Faist, "Comparison of CW and pulsed operation with a TE-cooled quantum cascade infrared laser for detection of nitric oxide at 1900 cm⁻¹," *Appl. Phys. B* **85**, 235–241 (2006).
23. A. Fried, Y. Wang, C. Cantrell, B. Wert, J. Walega, B. Ridley, E. Atlas, R. Shetter, B. Lefer, M. T. Coffey, J. Hannigan, D. Blake, N. Blake, S. Meinardi, B. Talbot, J. Dibb, E. Scheuer, O. Wingenter, J. Snow, B. Heikes, and D. Ehhalt, "Tunable diode laser measurements of formaldehyde during the TOPSE 2000: distributions, trends, and model comparisons," *J. Geophys. Res.* **108**, 8365–8386 (2003).
24. D. Richter, A. Fried, B. P. Wert, J. G. Walega, and F. K. Tittel, "Development of a tunable mid-IR difference-frequency laser source for highly sensitive airborne trace gas detection," *Appl. Phys. B* **75**, 281–288 (2002).
25. Y. Q. Li, K. L. Demerjian, M. S. Zahniser, D. D. Nelson, J. B. McManus, and S. C. Herndon, "Measurement of formaldehyde, nitrogen dioxide, and sulfur dioxide at Whiteface Mountain using a dual tunable diode laser system," *J. Geophys. Res.* **109**, D16S08 (2004).
26. G. Wysocki, Y. Bakhirkin, S. So, F. K. Tittel, C. J. Hill, R. Q. Yang, and M. P. Fraser, "Dual interband cascade laser based trace-gas sensor for environmental monitoring," *Appl. Opt.* **46**, 8202–8210 (2007).
27. K. Stimler, D. Nelson, and D. Yakir, "High precision measurements of atmospheric concentrations and plant exchange

- rates of carbonyl sulfide (COS) using mid-IR quantum cascade laser,” *Glob. Change Biol.* **16**, 2496–2503 (2010).
28. A. Fried, J. R. Drummond, B. Henry, and J. Fox, “Versatile integrated tunable diode laser system for high precision: application for ambient measurements of OCS,” *Appl. Opt.* **30**, 1916–1932 (1991).
 29. G. Wysocki, M. McCurdy, S. So, D. Weidmann, C. Roller, R. F. Curl, and F. K. Tittel, “Pulsed quantum-cascade laser-based sensor for trace-gas detection of carbonyl sulfide,” *Appl. Opt.* **43**, 6040–6046 (2004).
 30. J. Faist, F. Capasso, D. L. Sivco, C. Sirtori, A. L. Hutchinson, and A. Y. Cho, “Quantum cascade laser,” *Science* **264**, 553–556 (1994).
 31. C. Gmachl, F. Capasso, J. Faist, A. L. Hutchinson, A. Tredicucci, D. L. Sivco, J. N. Baillargeon, S. N. G. Chu, and A. Y. Cho, “Continuous-wave and high power pulsed operation of index-coupled distributed feedback quantum cascade laser at $\sim 8.5\ \mu\text{m}$,” *Appl. Phys. Lett.* **72**, 1430–1432 (1998).
 32. J. Faist, A. Tredicucci, F. Capasso, C. Sirtori, D. L. Sivco, J. N. Baillargeon, A. L. Hutchinson, and A. Y. Cho, “High-power continuous-wave quantum cascade lasers,” *IEEE J. Quantum Electron.* **34**, 336–343 (1998).
 33. F. Capasso, C. Gmachl, R. Paiella, A. Tredicucci, A. L. Hutchinson, D. L. Sivco, J. N. Baillargeon, A. Y. Cho, and H. C. Liu, “New frontiers in quantum cascade lasers and applications,” *IEEE J. Sel. Top. Quantum Electron.* **6**, 931–947 (2000).
 34. C. Gmachl, F. Capasso, D. L. Sivco, and A. Y. Cho, “Recent progress in quantum cascade lasers and applications,” *Rep. Prog. Phys.* **64**, 1533–1601 (2001).
 35. M. Beck, D. Hofstetter, T. Aellen, J. Faist, U. Oesterle, M. Illegems, E. Gini, and H. Melchior, “Continuous wave operation of a mid-infrared semiconductor laser at room temperature,” *Science* **295**, 301–305 (2002).
 36. D. R. Herriott, H. Kogelnik, and R. Kompfner, “Off axis paths in spherical mirror interferometers,” *Appl. Opt.* **3**, 523–526 (1964).
 37. D. R. Herriott and H. J. Schulte, “Folded optical delay lines,” *Appl. Opt.* **4**, 883–889 (1965).
 38. J. B. McManus, P. L. Kebabian, and M. S. Zahniser, “Astigmatic mirror multiple pass absorption cells for long pathlength spectroscopy,” *Appl. Opt.* **34**, 3336–3348 (1995).
 39. J. B. McManus, “Paraxial matrix description of astigmatic and cylindrical mirror resonators with twisted axes for laser spectroscopy,” *Appl. Opt.* **46**, 472–482 (2007).
 40. L.-Y. Hao, S. Qiang, G.-R. Wu, L. Qi, D. Feng, and Q.-S. Zhu, “Cylindrical mirror multipass Lissajous system for laser photoacoustic spectroscopy,” *Rev. Sci. Instrum.* **73**, 2079–3085 (2002).
 41. J. A. Silver, “Simple dense-pattern optical multipass cells,” *Appl. Opt.* **44**, 6545–6556 (2005).
 42. V. L. Kasyutich, “Laser beam patterns of an optical cavity formed by two twisted cylindrical mirrors,” *Appl. Phys. B* **96**, 141–148 (2009).
 43. J. B. McManus, M. S. Zahniser, D. D. Nelson, J. H. Shorter, S. Herndon, E. Wood, and Rick Wehr, “Application of QCLs to high precision atmospheric trace gas measurements,” *Opt. Eng.* (to be published).
 44. <http://www.esrl.noaa.gov/calnex/index.htm>.
 45. L. S. Rothman, A. Barbe, D. Chris Benner, L. R. Brown, C. Camy-Peyret, M. R. Carleer, K. Chance, C. Clerbaux, V. Dana, V. M. Devi, A. Fayt, J.-M. Flaud, R. R. Gamache, A. Goldman, D. Jacquemart, K. W. Jucks, M. J. Lafferty, J. Y. Mandin, S. T. Massie, V. Nemtchinov, D. A. Newnham, A. Perrin, C. P. Rinsland, J. Schroeder, K. M. Smith, M. A. H. Smith, K. Tang, R. A. Toth, J. Vander Auwera, P. Varanasi, and K. Yoshino, “The HITRAN molecular spectroscopic database: edition of 2000 with updates through 2001,” *J. Quant. Spectrosc. Radiat. Transfer* **82**, 5–44 (2003).
 46. P. Werle, R. Mucke, and F. Slemr, “The limits of signal averaging in atmospheric trace-gas monitoring by tunable diode-laser absorption spectroscopy (TDLAS),” *Appl. Phys. B* **57**, 131–139 (1993).